A compressible flow model for the air-rotor–stator dynamics of a high-speed, squeeze-film thrust bearing

J. E. GARRATT[1], K. A. CLIFFE[2]†, S. HIBBERD[2] AND H. POWER[3]

[1]University Technology Centre in Gas Turbine Transmission Systems, Faculty of Engineering, University of Nottingham, Nottingham, NG7 2RD, UK

[2]School of Mathematical Sciences, University of Nottingham, Nottingham, NG7 2RD, UK

[3]Fuels and Power Technology Research Division, Faculty of Engineering, University of Nottingham, Nottingham, NG7 2RD, UK

A compressible air-flow model is introduced for the thin film dynamics of a highly rotating squeeze-film thrust bearing. The lubrication approximation to the Navier–Stokes equations for compressible flow leads to a modified Reynolds equation incorporating additional rotation effects. To investigate the dynamics of the system, the axial position of the bearing stator is prescribed by a finite-amplitude periodic forcing. The dynamics of the squeeze-film are modelled in the uncoupled configuration where the axial position of the rotor is fixed. The coupled squeeze-film bearing dynamics are investigated when the axial position of the rotor is modelled as a spring-mass-damper system that responds to the film dynamics. Initially the uncoupled squeeze-film dynamics are considered at low operating speeds with the classical Reynolds equation for compressible flow. The limited value of the linearized small-amplitude results is identified. Analytical results indicate that finite-amplitude forcing needs to be considered to gain a complete understanding of the dynamics. Using a Fourier spectral collocation numerical scheme, the periodic bearing force is investigated as a nonlinear function of the frequency and amplitude of the stator forcing. High-speed bearing operation is modelled using the modified Reynolds equation. A steady-state analysis is used to identify the effect of rotation and the rotor support properties in the coupled air-flow–structure model. The unsteady coupled dynamics are computed numerically to determine how the rotor support structures and the periodic stator forcing influence the system dynamics. The potential for resonant rotor behaviour is identified through asymptotic and Fourier analysis of the rotor motion for small-amplitude, low-frequency oscillations in the stator position for key values of the rotor stiffness. Through the use of arclength continuation, the existence of resonant behaviour is identified numerically for a range of operating speeds and forcing frequencies. Changes in the minimum rotor–stator clearance are presented as a function of the rotor stiffness to demonstrate the appearance of resonance.

† Email address for correspondence: andrew.cliffe@nottingham.ac.uk

1. Introduction

A squeeze-film bearing makes use of a thin gas film to separate a rotating disk (rotor) from a coaxial stationary disk (stator) when subjected to imposed vertical displacements. The application of gas film bearings has the potential to provide improved bearing performance, particularly for high differential speed operation, in comparison to classical bearing designs involving liquid lubrication at low speeds.

Current applications of gas film bearings include the small bearings required in hard disk drives as reported by Witelski (1998), medium-scale industrial applications in generators and small engines and large-scale applications in prototype gas turbine aerospace engines as investigated by Malanoski & Waldron (1973).

Another technology that relies on air-film lubrication is the gas foil bearing. In such a device, a secondary compliant foil face is used to improve bearing performance and stability. Recent findings are reported by a number of authors, for example DellaCorte & Valco (2000) investigate foil journal bearings. The journal configuration is given extensive treatment by other authors, for example San Andrés & Kim (2009). Some work in the thrust bearing geometry is reported by Heshmat, Xu & Heshmat (2000) and Agrawal, Patel & Munson (2007) but most is focused on potential sealing applications.

The demands of new technology require bearings that can operate at very high rotational speeds, carry greater loads and maintain smaller clearances, as highlighted by Munson & Pecht (1992). These strict operational requirements make a comprehensive understanding of the air–rotor–stator dynamics vital. The current study considers gas film lubrication in a highly rotating environment for a squeeze-film thrust bearing configuration as the background to an investigation of other gas-lubricated bearings.

Early theoretical work on air-lubricated systems was reported by Taylor & Saffman (1957) in response to experimental results published by Popper & Reiner (1956), which were used to suggest that non-Newtonian properties of air needed to be considered. In this experiment, very large fluid pressures were observed in a system of two parallel disks separated by a thin air film and experiencing relative rotational and axial motion. By assuming the normal motion of one of the plates, Taylor and Saffman used the lubrication equations for compressible flow to predict these high pressures.

The theoretical modelling of so-called squeeze-films was formalized by Langlois (1962), where a classical Reynolds equation model was established to relate the compressible film pressure and thickness. Langlois reported analytical solutions to the squeeze-film problem in a number of general configurations including infinite rectangular films and axisymmetric disks when the thickness of the film oscillated periodically with a small amplitude. The latter of these solutions was an extension of the work of Taylor & Saffman (1957) and identified that for small-amplitude oscillations, the net force maintaining the disk separation (the squeeze-film force) is also of a small amplitude.

Salbu (1964) investigated the squeeze-film separating a pair of parallel rotating disks undergoing relative periodic motion in the axial direction. Using the theoretical Reynolds equation approach of Langlois (1962), Salbu extended previous results by modelling finite-amplitude disturbances. The corresponding experimental work on squeeze-film thrust bearings provided good agreement with the theoretical work. For large amplitudes, the pressure distribution exhibited peaks when the rotor–stator clearance was minimized, resulting in a positive net axial force that provided a load-carrying capacity for squeeze-film bearings. This feature is also observed by Stolarski

& Chai (2006*a*), who conclude that the only way to generate a load-carrying force in a thin air film without pressurization is through normal squeeze motion.

In contrast to the modelling of compressible air lubricating films, Parkins & Stanley (1982) and Stolarski & Chai (2006*a*) both report results for an incompressible oil film. Theoretical and experimental results show that, owing to the approximately incompressible nature of oil, the generation of a positive film force is severely restricted. Clearly, the load-carrying property of a squeeze-film is due to the compressible nature of the air film that responds in a nonlinear manner to the periodic normal forcing imposed on the system, a feature neglected by the linearized approach. This conclusion is reinforced by Fourka, Tian & Bonis (1996), who employed a finite-element computational scheme to solve the full nonlinear Reynolds equation in parallel to corresponding analytical and experimental analyses. The primary focus of the work was to investigate the stability of gas-lubricated bearings, but it was also concluded that relevant models needed to include the nonlinear compressibility effects in order to adequately predict the experimental results.

In many studies of gas squeeze-films, the air film between the bearing plates is analysed when the motion of the plates is fully prescribed; however, a number of authors consider the full problem of a structure–air-film coupling when the axial position of the supported mass or rotor is unknown. Minikes & Bucher (2003) carried out a detailed analysis of this coupled problem when a mass is levitated by squeeze-film action generated by an oscillating piezoelectric disk. The coupled dynamics were seen to be quite different to those predicted by the uncoupled analysis in the literature, motivating the current study of both models.

The work of Hasegawa & Izuchi (1996) investigated how the load-carrying capacity of an externally pressurized slider bearing was modified through the inclusion of air film inertia. They carried out a dimensional analysis of the steady Navier–Stokes equations for compressible flow that at leading order reduced to the steady lubrication equations. Through a perturbation analysis, they showed that an increased load-carrying capacity and enhanced bearing performance was predicted by the inclusion of first-order inertia terms. Through the use of an average inertia approximation, a modified Reynolds equation was formulated for squeeze-film action by Stolarski & Chai (2008). The air film pressure distributions in a square geometry were found, and when compared to their own previous results in the absence of inertia, Stolarski & Chai (2006*b*) showed that inertia effects do not modify the load-carrying capacity. Using an averaged inertia method, Brunetière & Tournerie (2006) investigated the effect of inertia on the fluid flow within a hydrostatic seal. In this annular pressurized geometry, it was shown numerically that the effect of inertia on the steady seal clearance was small; however, the inertia effects significantly modified the leakage from the seal. Their results are based on a comparison between the inertia model and the inertialess model presented in full detail by Brunetière, Tournerie & Frêne (2003*a*, *b*). In general, the results presented in the literature are varied; it appears that the overall effect of inertia is determined by both the geometry in which the air lubricating film is employed and the extent to which the axial, radial and azimuthal components of the inertia contribute to the flow. This observation suggests that the classical inertialess Reynolds equation will not be appropriate for every configuration of thin lubricating films, so a case-by-case approach must be adopted.

The current study develops a modified Reynolds equation model for the squeeze-film that incorporates the effect of radial inertia to provide results for highly rotating configurations. By fully prescribing the rotor–stator motion, the modified Reynolds equation is used to investigate the basic squeeze-film dynamics. The current
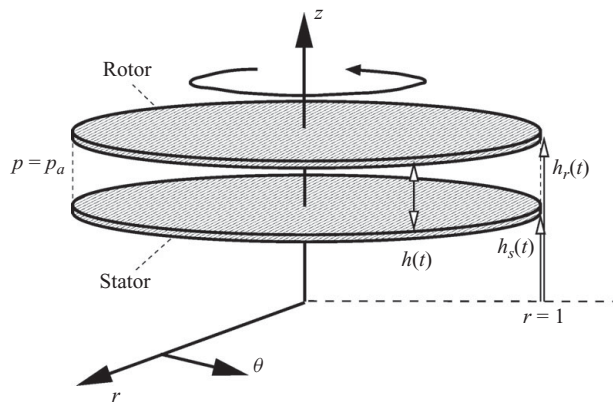
FIGURE 1. Geometry of a squeeze-film thrust bearing in a dimensionless cylindrical coordinate system (r, θ, z).

investigation extends the dynamics due to finite-amplitude oscillations to the limit of low- and high-frequency oscillations in the bearing clearance.

To offer further insight into the full air–rotor–stator dynamics of a squeeze-film bearing the modified Reynolds equation is employed to model the bearing dynamics when the motion of the stator is fully prescribed and the rotor moves axially in response to the dynamics of the film, subject to mechanical stiffness and damping constraints. The current study sheds light on the film–structure coupling and the influence of both the air film and bearing structure properties for a range of different forcing amplitudes and frequencies and at a number of high operating speeds.

Numerical solutions to the periodic uncoupled and coupled squeeze-film bearing problems can be obtained from a Fourier spectral collocation numerical scheme. Additionally, using the method of arclength continuation, branches of solutions provided by the spectral collocation scheme are tracked over the parameter space to identify the bearing behaviour as a function of the modelling parameters, particularly in the extremes of the parameter range where other methods fail. Details of the numerical methods and their accuracy for both the uncoupled and coupled squeeze-film bearing problems are given by Garratt *et al.* (2010).

The modified Reynolds equation approach to the modelling of air-lubricated bearings in this study provides a background to the study of other similar devices incorporating high-speed effects. The physical processes driving the dynamics are expected to be common to a number of configurations and applications, for example the use of air-riding films as alternative means for supporting a load and stabilizing the behaviour of mechanical components; for example see Witelski (1998) and Munson & Pecht (1992). Additionally, the oil-free operating environment is attractive to those involved with the development of micro-turbomachinery and other precision engineering systems.

2. Problem formulation

A squeeze-film thrust bearing is designed to carry a load in the direction normal to the bearing plates with an air squeeze-film maintaining the rotor–stator separation. Figure 1 shows a sketch of the geometry of a typical parallel plate squeeze-film thrust bearing in a dimensionless cylindrical coordinate system (r, θ, z). The relative

axial positions of the rotor and stator are $h_r(t)$ and $h_s(t)$, respectively, so that the rotor–stator clearance is $h = h_r - h_s$. The rotor and stator are taken to remain parallel and are in relative tangential motion, but a normal motion exists so that the rotor moves axially relative to the stator. At the edge of the bearing, the air pressure is the dimensionless ambient pressure p_a.

To investigate the dynamics of the squeeze-film, the motion of the stator is prescribed by a periodic oscillation

$$h_s(t) = \epsilon \sin t, \qquad (2.1)$$

having a dimensionless amplitude of ϵ. The time scale of the problem has been chosen as ω^{-1} (s), where ω (Hz) is the frequency of the forced oscillations and the units are in parentheses. This forced motion represents mechanical vibrations and imperfections in the operating environment that may act to destabilize the rotor–stator motion of the bearing. To initially compare with the results in the literature, the rotor's position is fixed at the height of $h_r(t) = 1$ so that the rotor–stator clearance becomes

$$h(t) = 1 - \epsilon \sin(t). \qquad (2.2)$$

This expression for the rotor–stator clearance simplifies the analysis, but the results of Minikes & Bucher (2003) and Brunetière, Tournerie & Frêne (2002) indicated that such models provide only partial insight into the full air–rotor–stator dynamics.

To extend earlier models of squeeze-film bearing dynamics, a model for the rotor behaviour is considered where rotor is free to move axially in response to the air flow and where the rotor–stator clearance is given more generally by

$$h(t) = h_r(t) - \epsilon \sin t. \qquad (2.3)$$

The axial rotor displacement is modelled as a spring-mass-damper system using Newton's second law and experiences a force due to the pressure within the air film given in dimensionless variables by

$$\frac{d^2 h_r}{dt^2} + 2\zeta \sqrt{S_p}\frac{dh_r}{dt} + S_p(h_r - 1) = \alpha F(t), \qquad (2.4a)$$

where $\zeta = \hat{D}_a/(2\sqrt{m\hat{S}_p})$ is the dimensionless damping ratio in terms of the dimensional damping and stiffness parameters $\hat{D}_a$ (N s m^{-1}) and $\hat{S}_p$ (N m^{-1}), respectively, and the rotor mass m (kg). The natural frequency of the dimensional system is defined as $\phi_0 = \sqrt{\hat{S}_p/m}$ (Hz) and it is noted that the dimensionless spring constant is the ratio of the stator forcing frequency to the natural frequency of the dimensional system $S_p = (\phi_0/\omega)^2$. The strength of the force coupling, incorporating the effect of the rotor mass, is parameterized by $\alpha = (\mu U/m\omega^2)(h_0^3/R^3)$, where the dimensional bearing radius is R (m). The dimensionless axial force due to the hydrodynamic pressure for a squeeze-film bearing is

$$F(t) = 2\pi \int_0^1 (p - p_a)\, r\, dr, \qquad (2.4b)$$

where p_a is the dimensionless ambient pressure. For convenience, the equilibrium height of the rotor has been chosen to incorporate the effect of the rotor mass so that $h_0 = H - mg/\hat{S}_p$ (m), where the equilibrium rotor position in the absence of gravity and rotation is $\hat{h}_r = H$ (m).

The governing equations for the air flow between the rotor and stator are the Navier–Stokes equations for an isothermal compressible fluid. The relative importance

of compressible flow characteristics is quantified by the Mach number. It is expected that for exceptional combinations of the rotation speed and bearing width, the Mach number could exceed one, indicating the importance of compressibility effects. More generally, the Mach number will be small; however, Taylor & Saffman (1957) indicated that compressibility effects are also significant when a thin layer of fluid is forced into a small space. Their paper went further and confirmed that the compressible flow model gives the best correspondence with experimental work in this field and is followed by many later studies, for example Salbu (1964) and Stolarski & Chai (2006*a*).

To characterize the relative importance of fluid inertia, it is useful to define the radial and azimuthal Reynolds numbers as

$$Re_U = \frac{\rho_0 R U}{\mu} \quad \text{and} \quad Re_\Omega = \frac{\rho_0 \Omega R^2}{\mu}, \tag{2.5}$$

respectively. In the above, ρ_0 (kg m^{-3}) and U (m s^{-1}) are a typical air density and radial velocity, respectively. The dynamic viscosity of air is μ (bar s) and Ω (r.p.s.) is the rotation rate for the rotor. A Reynolds number ratio is defined as

$$Re^* = \frac{Re_\Omega}{Re_U} = \frac{\Omega R}{U}. \tag{2.6}$$

Taking the equilibrium bearing clearance h_0 (m) and the radius of the rotor R (m) as typical vertical and radial length scales, a bearing aspect ratio is defined as

$$\delta_0 = \frac{h_0}{R}. \tag{2.7}$$

In the operation of a squeeze-film bearing typically the rotor–stator clearance is very small relative to the radius of the disks so that $\delta_0 \ll 1$.

Classical lubrication theory neglects the effects of fluid inertia by requiring a small reduced Reynolds number. However, for bearings operating at very high speeds of rotation, the centrifugal inertia term will not necessarily be negligible.

A viscous pressure scale is employed and the leading-order terms in the compressible flow Navier–Stokes momentum equations are retained. Applying no-slip velocity boundary conditions, the radial and azimuthal velocities are then readily found, and these velocities and the continuity equation are integrated across the film thickness. Applying the rigid-surface conditions to this expression yields the axisymmetric modified Reynolds equation

$$\sigma \frac{\partial}{\partial t}(ph) - \frac{h^3}{12r}\frac{\partial}{\partial r}\left(pr\frac{\partial p}{\partial r}\right) + \frac{\lambda}{40K}\frac{h^3}{r}\frac{\partial}{\partial r}(r^2 p^2) = 0, \tag{2.8}$$

where $\sigma = R\omega/U$ is the squeeze number.

The formulation of (2.8) from an asymptotic analysis is provided in the Appendix. The parameter $\lambda = Re_U \delta_0^2 Re^{*2}$ quantifies the effect of flow inertia because of high-speed rotation. The fluid density relative to the pressure is characterized by the modified gas constant $K = (\rho_0 k_b \tau h_0^2)/(\mu m_a R U)$, where k_b (J K^{-1}) is the Boltzmann constant, m_a (kg) is the mass of air and τ (K) is the fluid temperature.

Neglecting edge effects, the squeeze-film is subject to a constant ambient pressure p_a at the periphery of the bearing structure so that

$$p = p_a \quad \text{at} \quad r = 1. \tag{2.9a}$$

In this axisymmetric model, a pressure symmetry condition is applied at the origin, requiring that

$$\frac{\partial p}{\partial r} = 0 \quad \text{at} \quad r = 0. \tag{2.9b}$$

The modified Reynolds equation (2.8) expresses the relationship between the fluid pressure $p(r,t)$ and the film thickness $h(t)$. The equation differs from the classical Reynolds equation for compressible flow through the inclusion of an additional term parameterized by λ. The case when $\lambda = 0$ corresponds to low-speed operation with the classical Reynolds equation, reported by Langlois (1962) and Gross (1980) for example. A non-zero speed parameter introduces centrifugal inertia effects into the squeeze-film bearing problem. Such high-speed cases have been considered before but in this study their effects are combined with those arising from air compressibility, finite-amplitude forcing and coupled rotor motion.

When the rotor–stator clearance is fully prescribed by (2.2), the modified Reynolds equation (2.8) is solved subject to conditions (2.9), which together comprise the uncoupled problem for periodic squeeze-film dynamics in a highly rotating environment. In the configuration where the rotor motion is not fixed, the film pressure and thickness are related by the modified Reynolds equation (2.8), subject to conditions (2.9), and requires the simultaneous solution of (2.8) and (2.4). This system makes up the coupled problem for the periodic air–rotor–stator dynamics of a squeeze-film bearing with high-speed rotation.

3. Uncoupled dynamics at low operating speeds ($\lambda = 0$)

In the first instance, taking $\lambda = 0$ the modified Reynolds equation (2.8) reduces to the classical Reynolds equation. Taylor & Saffman (1957) report a leading-order asymptotic solution using Bessel functions for the pressure distribution within a squeeze-film for a small-amplitude forced motion given by (2.2). In the operation of squeeze-film bearings, a crucial aspect of the design concerns its load-carrying ability. After extensive calculations, Langlois (1962) found a closed-form expression for the force on the bearing surface in the large squeeze number limit. To evaluate the load-bearing capacity for more general squeeze numbers, the small-amplitude result of Taylor & Saffman (1957) can be numerically integrated over the rotor surface using a composite trapezium rule. It can be observed that for this small-amplitude case, the force profiles are sinusoidal and become in-phase with the stator motion for large squeeze numbers. Crucially, it is noted that the average force is zero for all small-amplitude forcing.

3.1. *Low-frequency stator oscillations, $\sigma \ll 1$*

Solving the Reynolds equation with $\sigma \ll 1$, an asymptotic pressure distribution to first order is

$$p(r,t) = p_a + \sigma \frac{3\epsilon \cos t}{(1 - \epsilon \sin t)^3} \left(1 - r^2\right) + O\left(\sigma^2\right) \propto -\frac{\mathrm{d}h}{\mathrm{d}t} \frac{1}{h^3}. \tag{3.1}$$

Integrating the pressure distribution (3.1) over the surface of the rotor relative to the ambient pressure gives the corresponding force on the rotor as

$$F(t) = \frac{3\pi\sigma\epsilon \cos t}{2\left(1 - \epsilon \sin t\right)^3} + O\left(\sigma^2\right). \tag{3.2}$$
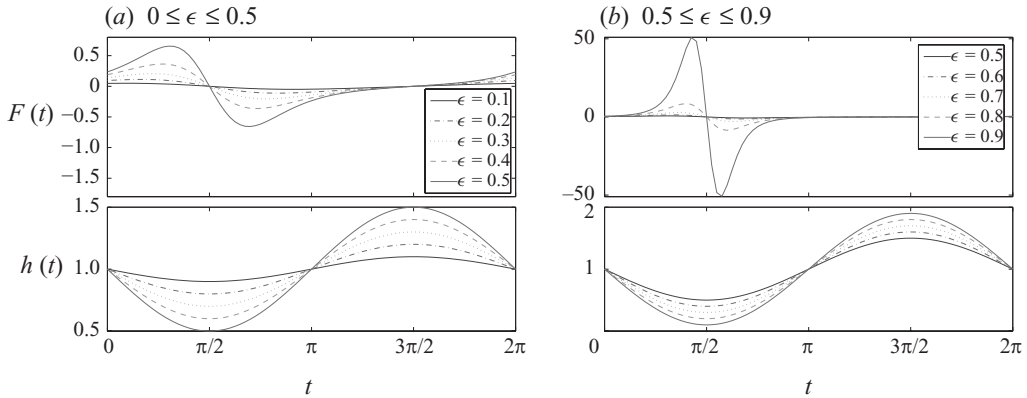
FIGURE 2. Force profiles from low-frequency ($\sigma \ll 1$) asymptotics; $\sigma = 0.1$ and $p_a = 1$.

This load-carrying force is in-phase with the speed of the rotor–stator oscillations $\mathrm{d}h/\mathrm{d}t = -\epsilon\cos t$. This observation was made by Salbu (1964) and identified as viscous damping behaviour. Figure 2 shows the force profiles and the rotor–stator clearance profiles for increasing forcing amplitudes of $0 \leqslant \epsilon \leqslant 0.5$ and $0.5 \leqslant \epsilon \leqslant 0.9$ in figures 2(a) and 2(b), respectively. Despite the presence of large-amplitude peaks in the force the average force over one period of oscillation is zero. It is suggested that in this low-frequency case, the speed of compression is small, resulting in the air being driven out of the bearing rather than in the compression of the air, even in the case of large-amplitude forcing.

3.2. High-frequency stator oscillations, $\sigma \gg 1$

Taking the large squeeze number limit $\sigma \gg 1$, i.e. high-frequency plate oscillations, the leading-order inner solution within a singular perturbation analysis of the Reynolds equation is given by

$$p = \frac{C}{h(t)} + O\left(\frac{1}{\sigma}\right), \tag{3.3}$$

for a constant C. This is the so-called 'Ph solution'; however, this pressure field does not satisfy the peripheral boundary condition (2.9a) and suggests that an outer boundary-layer solution exists. Defining the boundary-layer variable x by $r = 1 - (1/\sqrt{12\sigma})x$, the Reynolds equation becomes

$$\frac{\partial}{\partial t}(ph) - h^3 \frac{\partial}{\partial x}\left(p\frac{\partial p}{\partial x}\right) + O\left(\frac{1}{\sqrt{\sigma}}\right) = 0. \tag{3.4}$$

For small-amplitude oscillations ($\epsilon \ll 1$), the outer solution resulting from (3.4) is given by

$$p = p_a \left(1 - \epsilon\sin(t)\left(\exp(-\sqrt{(6\sigma/p_a)}(1-r))\cos\left(\sqrt{\frac{6\sigma}{p_a}}(1-r)\right) - 1\right)\right.$$

$$\left. + \epsilon\cos(t)\left(\exp(-\sqrt{(6\sigma/p_a)}(1-r))\sin\left(\sqrt{\frac{6\sigma}{p_a}}(1-r)\right)\right)\right) + O\left(\epsilon^2, \frac{\epsilon}{\sqrt{\sigma}}\right). \tag{3.5}$$

The matching of (3.3) and (3.5) requires that $C = p_a$. This pressure distribution is presented in figure 3 at a number of points in the time period and shows a radially
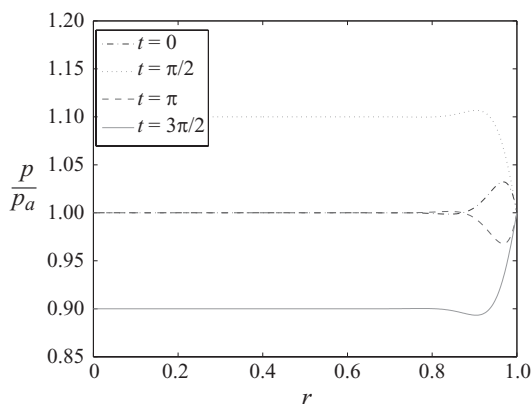
FIGURE 3. High-frequency ($\sigma \gg 1$) asymptotic pressure distribution; $\sigma = 100$, $p_a = 1$ and $\epsilon = 0.1$.

uniform pressure in the bulk and a rapidly changing nonlinear pressure in the boundary layer.

The periodic bearing force arising because of this asymptotic pressure distribution is

$$F(t) = \epsilon \pi \sin t + O\left(\epsilon^2, \frac{\epsilon}{\sqrt{\sigma}}\right), \tag{3.6}$$

giving an average force of zero in this small-amplitude case. This result demonstrates that a load-carrying ability cannot be generated by a high-frequency small-amplitude stator oscillation alone, suggesting that a significant degree of fluid compression must occur before a load-carrying force is generated.

3.3. *Squeeze-film dynamics due to finite-amplitude forcing*

Salbu (1964) presented some finite-amplitude forcing solutions to the Reynolds equation; however, limitations in the numerical scheme employed did not allow a complete investigation of finite-amplitude effects over a range of squeeze numbers. To investigate the effect of finite-amplitude forcing in the current study for more general frequencies of oscillation, the dynamics of the system are computed using a Fourier spectral collocation scheme.

Figure 4(a) shows the numerical force profiles corresponding to a large-amplitude forcing $\epsilon = 0.9$ for a range of squeeze numbers. Through increasing the squeeze number the force profile displays an asymmetric peak generated by the compression of the film at the point when the rotor–stator clearance is least.

To characterize the relationship between the load-carrying ability and the film compression, (3.3) with $C = p_a$ is used to approximate the pressure throughout the bearing for larger-amplitude oscillations with large squeeze numbers. The corresponding leading-order axial force is

$$F(t) = \pi p_a \left(\frac{1 - h(t)}{h(t)}\right) + O\left(\frac{1}{\sigma}\right) = \pi p_a \left(\frac{\epsilon \sin t}{1 - \epsilon \sin t}\right) + O\left(\frac{1}{\sigma}\right). \tag{3.7}$$

This force is shown in figure 4(b) for a range of stator oscillation amplitudes.

The approximate Boyle's law force profile in figure 4(b) for $\epsilon = 0.9$ underpredicts the numerically computed profile shown in figure 4(a) for $\sigma = 20$ at $t = 0$ despite showing qualitative agreement with the shape of the profiles. This difference arises because the spectral collocation scheme requires a periodic solution and allows a
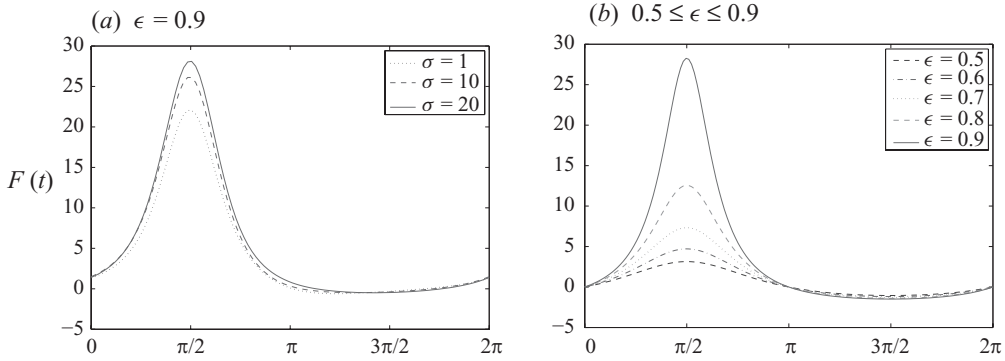
FIGURE 4. Force profiles: (*a*) numerical solutions; (*b*) Boyle's pressure law force, $\sigma \gg 1$ and $p_a = 1$.

super-ambient pressure at $t = 0$. For the analytical pressure in (3.3), $C = p_a$, so that at $t = 0$ the pressure is only atmospheric. This difference causes an underprediction of the average squeeze-film force.

Despite quantitative differences between the results computed numerically and those predicted by Boyle's law, the profiles in each case display similarities that aid the classification of squeeze-film dynamics. Typically, Boyle's law is used to model the compression of air in a closed cylinder where the mass of air within the cylinder remains constant and the flow is driven by the compression of the air from above or below. The characteristics of Boyle's law observed in the numerically computed cases indicate that for high-frequency stator oscillations, the air is compressed at such a rate that there is no time for the air to overcome the viscous forces opposing the outwards flow and thus the majority of the air remains within the bearing and undergoes significant compression, a result corroborated by Salbu (1964). This compression creates an asymmetric force profile and generates a load-carrying force. To quantify this behaviour the average force $\bar{F}$ is plotted in figure 5 as a function of the forcing amplitude and for a range of squeeze numbers. The results in this figure indicate how a combination of large-amplitude and high-frequency oscillations can be used to develop a load-carrying force through squeeze-film action.

4. Uncoupled dynamics at high operating speeds ($\lambda > 0$)

The effect of fluid inertia in air lubricated systems for selected geometries is presented by a number of authors including Brunetière & Tournerie (2006) and Stolarski & Chai (2008). Results suggest that the influence of inertia is not always significant and is typically dependent on the geometry of the specific configuration. The effect of inertia in a squeeze-film bearing remains unreported, motivating an investigation of a modified Reynolds equation (2.8) incorporating centrifugal inertia effects arising because of high-speed rotation.

The initial analysis of the high-speed squeeze-film considers the steady-state problem from (2.8). It can be shown that for non-zero values of the speed parameter, the steady air pressure within the bearing is less than atmospheric throughout and is at a minimum at the centre of the bearing.

The corresponding steady force is

$$F = \pi p_a \left(\frac{20K}{3\lambda} \left(1 - e^{-3\lambda/20K} \right) - 1 \right). \tag{4.1}$$
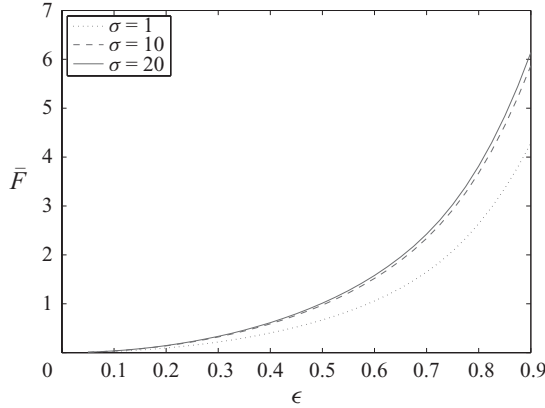
FIGURE 5. Numerically computed average force within a squeeze-film bearing over one
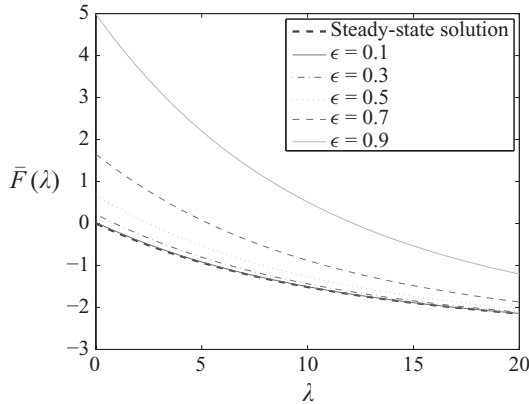period of oscillation; $p_a = 1$.

FIGURE 6. Numerically computed time-averaged force; $\sigma = 1$ and $p_a = 1$.

The interior sub-ambient pressure produces a negative force acting on the rotor that
attempts to draw the rotor closer to the stator. Additionally, for increasing values
of the speed parameter, the force tends towards a maximum negative limit value of
$-\pi p_a$.

To compute solutions to the full unsteady problem, a Fourier spectral collocation
numerical scheme is employed. To characterize the basic effect of inertia, the time-
averaged force $\bar{F}$ is shown in figure 6 for a range of speed parameter values λ and for
selected oscillation amplitudes of $\epsilon = 0.1, 0.3, 0.5, 0.7$ and 0.9, and the force predicted
by the steady solution is included for comparison. Each of the results shows that high-
speed rotation reduces the force; on the other hand, the effect of increased oscillation
amplitude is increased force, and the results for a large-amplitude oscillation ($\epsilon = 0.9$)
show the potential for a positive average force for sufficiently low speeds of rotation.
The positive values of the force indicate that the squeeze-film compressibility force
exceeds the suction force caused by rotation.

To observe the effect of higher-frequency oscillations within this high-speed regime,
the time-averaged force within the bearing was computed numerically for a range
of squeeze numbers and speed parameters. For small-amplitude oscillations $\epsilon = 0.1$,
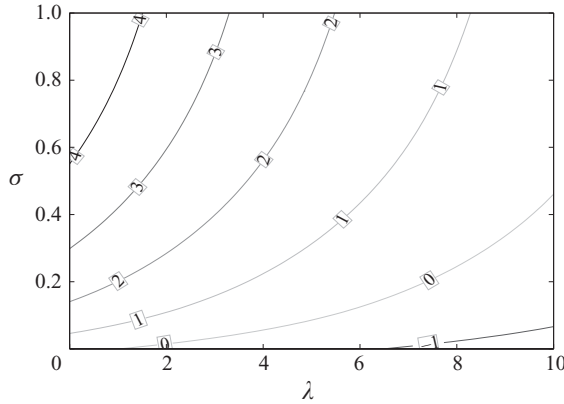
FIGURE 7. Contours of the time-averaged force computed numerically; $\epsilon = 0.9$ and $p_a = 1$.

the average squeeze-film force is insensitive to changes in the squeeze number and decreases uniformly with increasing speed parameter, as predicted in the steady-state analysis discussed above. The contours of the time-averaged force for a finite-amplitude oscillation $\epsilon = 0.9$ are shown in figure 7, and the effect of varying the squeeze number is seen to be significant. For the smallest values of the squeeze number, the film force is negative for all non-zero rotation speeds; however, increased values of the squeeze number cause an increased average force. This increase in average force produces a significant region in the parameter space where a positive film force is generated. This force arises because of the high frequency (large squeeze number) and large amplitude of the oscillations and is attributed to the increased energy being applied to the system through the repeated compression of the air film that generates the squeeze-film compressibility force.

The complexity of figure 7 demonstrates the importance of considering large-amplitude oscillations when considering the dynamics of squeeze-films. It is only in this regime that the nonlinear aspects of this problem become significant and the dynamics of the flow become sensitive to variations in the physical parameters, features that are not apparent from linearized results in this area. A full understanding of the dynamics in this operating regime is critical to the successful operation of air-lubricated devices.

5. Coupled bearing dynamics

The full air–rotor–stator dynamics of a squeeze-film bearing are now modelled when the axial motion of the stator is prescribed and the film dynamics drive the coupled rotor motion. The axial position of the forced stator motion is taken as $h_s(t) = \epsilon \sin t$, and the subsequent rotor position $h_r(t)$ gives the rotor–stator clearance to be $h(t) = h_r(t) - \epsilon \sin t$.

5.1. *Steady-state coupled behaviour*

In a steady state $h_s = 0$ and the steady force F is given by (4.1), then from (2.4) the rotor position becomes

$$h_r(\lambda) = 1 - \frac{\alpha \pi p_a}{S_p} \left(1 - \frac{20K}{3\lambda} \left(1 - e^{-3\lambda/20K} \right) \right) \quad \text{for } \lambda > 0. \tag{5.1}$$
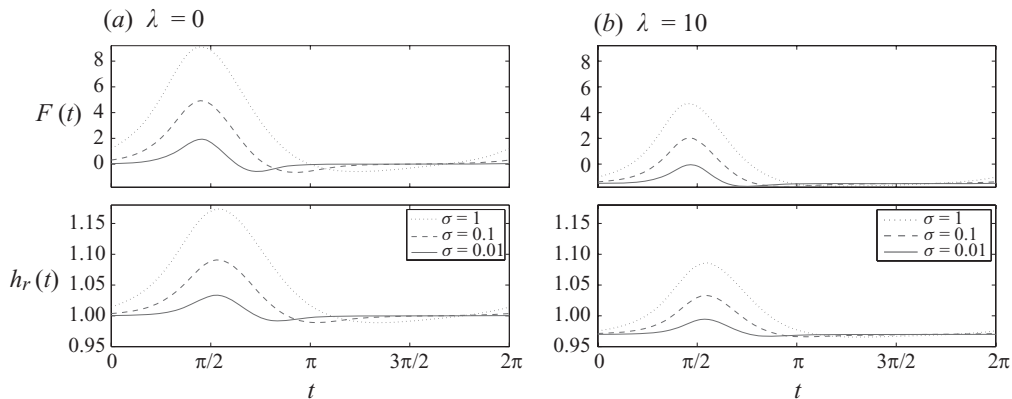
FIGURE 8. Numerical force and rotor position profiles; $\epsilon = 0.9$, $p_a = 1$, $\zeta = 1$, $S_p = 50$ and $\alpha = 1$.

In all cases, an increased rate of rotation decreases the rotor height whilst increased rotor stiffness S_p reduces the set-down of the rotor. For high values of the speed parameter, the rotor set-down position tends towards a finite limit of $1 - (\alpha \pi p_a / S_p)$, depending on both the stiffness of the rotor support and the coupling parameter.

5.2. *Unsteady coupled dynamics*

5.2.1. *Effect of forcing amplitude and frequency*

Solutions to the unsteady problem are computed for a number of amplitudes of stator oscillation ϵ using a Fourier spectral collocation method. From these numerical results the time-averaged rotor position over one period can be computed numerically using the trapezium rule. This average position is modified by both the speed parameter and the forcing frequency, most significantly for finite amplitudes of stator forcing in a manner analogous to the behaviour shown for the average force in figure 7.

To gain a full understanding of the bearing dynamics, the unsteady force and rotor position profiles are considered. Examples of solutions to the modified Reynolds equation (2.8) and the rotor position equation (2.4) are given for a number of values of the squeeze number. Figures 8(*a*) and 8(*b*) show results for a large-amplitude oscillation $\epsilon = 0.9$ in the inertialess case $\lambda = 0$ and the high-speed case $\lambda = 10$, respectively.

The force and rotor position profiles in figure 8 display significant asymmetric peaks at the point of greatest stator height and maximum film compression. At the same point in time, the rotor position undergoes a large deflection away from the stator because of the increased force acting on the rotor due to the film compression. In both figures it is seen that increased values of the squeeze number result in forces of a greater magnitude and correspondingly a greater degree of rotor deflection. Comparing the two figures it is clear that the high-speed rotation induces a damping force within the system that lessens the magnitude of the maxima and minima of the profiles in the high-speed case. Additionally, for the high-speed rotation in figure 8(*b*), a negative force is seen over the whole period in the small squeeze number case $\sigma = 0.01$, resulting in a rotor position less than the equilibrium position. Importantly, it is noted that for the higher-frequency stator oscillations with $\lambda = 10$, there is a balance between the negative forces that are generated because of high operating speeds and the positive 'squeeze' force due to the compression of the air film.
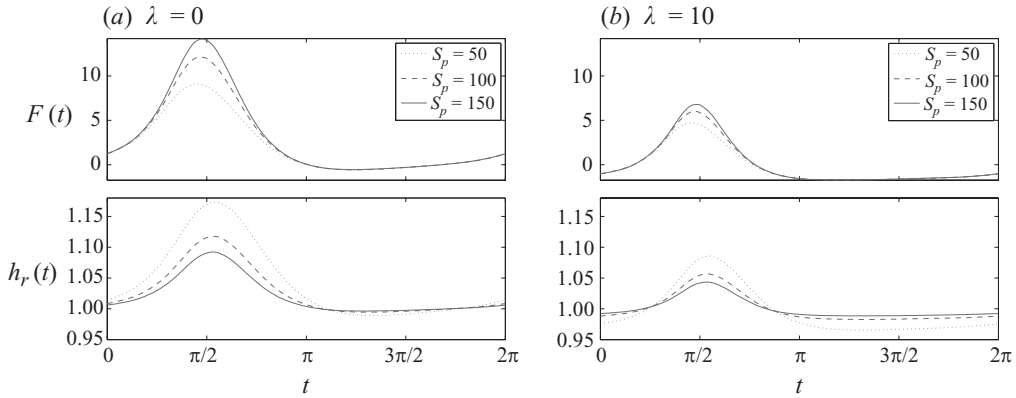
FIGURE 9. Numerical force and rotor position profiles; $\epsilon = 0.9$, $\sigma = 1$, $p_a = 1$, $\zeta = 1$ and $\alpha = 1$.

5.2.2. *Effect of rotor support properties*

The dynamics of the rotor are moderated by the properties of the rotor support structures, the damping ratio ζ, spring stiffness S_p and the coupling parameter α. These parameters are now considered in greater detail to investigate more completely the role they play in determining the bearing dynamics.

Figure 9 shows the force and rotor position profiles plotted for one period of oscillation and for a selected range of spring stiffnesses. These figures correspond to the inertialess case $\lambda = 0$ and the high-speed case $\lambda = 10$, respectively. For the smallest stiffness considered in figure 9(a) at $t = \pi/2$, the rotor motion displays the greatest deflection from the initial equilibrium rotor position of unity. This deflection decreases for the increased stiffness values of $S_p = 100$ and 150 by increasing the resistance of the rotor to axial motion due to film compression. The force profiles shown in figure 9(a) show the opposite behaviour to the rotor because the largest force is generated when the stiffness is greatest and the rotor deflection is most restricted. This produces a smaller minimum clearance than for the low stiffness case and brings about a greater degree of film compression and force generation.

In figure 9(b) the rotor position and force profiles are shown for the high-speed rotation case $\lambda = 10$. The trends observed in the low-speed case are displayed; however, the response of the rotor is modified. The maximum deflection occurring at $t = \pi/2$ is seen in the low stiffness case $S_p = 50$, but for most of the time the low stiffness case shows a significant decrease in the rotor position in comparison to the medium and large stiffness results. This behaviour is attributed to the high-speed rotation that modifies the rotor position when there is only a small restoring spring force. Increasing stiffnesses would maintain the rotor close to the equilibrium position and reduce the downwards motion because of the high-speed rotation.

The effect of mechanical damping is displayed in figure 10 with a comparison of the results for three values of the damping ratio ζ in the case of large-amplitude oscillations ($\epsilon = 0.9$). In the undamped case ($\zeta = 0$), the rotor height reaches maximum amplitude at the point of maximum stator height, and correspondingly the film force is least. For increased values of the damping ratio, the amplitude of the rotor deflection is reduced and the film force increases. Additionally, the increased levels of damping cause a phase shift between the rotor and stator motion. Typically, for a damping ratio less than unity, such a system should display oscillations of a frequency $\sqrt{S_p}$.
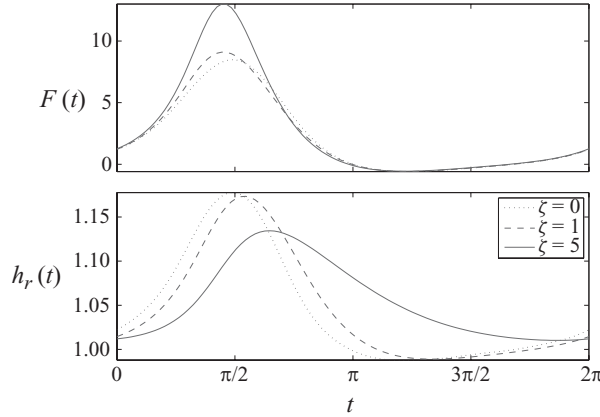
FIGURE 10. Numerical force and rotor position profiles; $\epsilon = 0.9$ with $\sigma = 1$, $p_a = 1$, $\lambda = 0$, $S_p = 50$ and $\alpha = 1$.
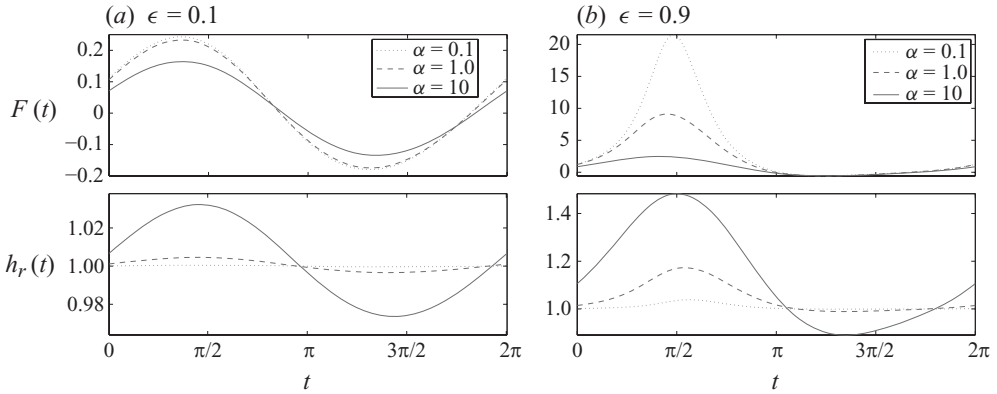

FIGURE 11. Numerical force and rotor position profiles; $\sigma = 1$, $p_a = 1$, $\lambda = 0$, $S_p = 50$ and $\zeta = 1$.

However, owing to the periodic forcing, such undamped oscillations do not exist for non-integer values of $\sqrt{S_p}$. Furthermore, the damping properties of the coupled air flow may damp out any oscillations appearing in the rotor height.

The results in figures 9(a), 9(b) and 10 demonstrate the significance of the coupled rotor–structure model, particularly for large-amplitude forcing. The behaviour is investigated further by analysing how the coupling parameter α changes the air–rotor–stator dynamics in both the small- and large-amplitude regimes typified by $\epsilon = 0.1$ and 0.9.

Increased values of the coupling parameter, corresponding to a reduced rotor mass, increase the amplitude of the rotor motion shown in figure 11(a). Additionally, in the large-amplitude case in figure 11(b), increasing the coupling parameter reduces the force profile. As the amplitude of stator oscillation is increased, the changes in the coupling parameter bring about significant changes in the force profile as well as the rotor position.

5.3. *Identification of resonant dynamics*

In the current squeeze-film bearing analysis, a forced oscillatory stator motion has been modelled to represent a vibration acting on the system. The potential for resonance due to this forced vibration is now considered.

5.3.1. *Analysis for small-amplitude, low-frequency forcing*

For low-frequency oscillations in the stator position ($\sigma \ll 1$), an asymptotic solution for the no-inertia case ($\lambda = 0$) was given by (3.1). In this case, the dynamics of the air flow become uncoupled from the rotor motion, so this pressure remains valid in the coupled model.

The axial rotor displacement h_r in the absence of damping ($\zeta = 0$) and satisfying (2.4) for small amplitudes of stator displacement ($\epsilon \ll 1$) is given by the fourth-order expansion

$$
\begin{aligned}
h_r \sim\ & 1 + \epsilon\sigma \frac{3\pi\alpha \cos t}{2\,(S_p - 1)} + \epsilon^2\sigma \frac{9\pi\alpha \cos t}{2\,(S_p - 4)} \sin t \\
& + \epsilon^3\sigma \frac{9\pi\alpha \cos t}{(S_p - 9)\,(S_p - 1)} \left((S_p - 1) \sin^2 t - 2 \right) \\
& + \epsilon^4\sigma \frac{15\pi\alpha \cos t}{(S_p - 16)\,(S_p - 4)} \left((S_p - 4) \sin^3 t - \sin t \right).
\end{aligned}
\tag{5.2}
$$

This expression becomes singular for $S_p = 1, 4, 9, 16$ because of the emergence of a higher-order term that restricts the validity of the expansion. Each additional term corresponds to higher-order terms that increase in frequency with the order of the term. To gain further insight into the presence of these singular dynamics, an approximate Fourier series analysis is conducted by expressing the force in terms of Fourier coefficients $\hat{F}_k$ so that $F(t) = \sum_k e^{ikt} \hat{F}_k$. Writing the rotor position as a Fourier expansion $h_r(t) = 1 + \sum_k e^{ikt} \hat{h}_k$, it can be shown that the Fourier coefficients of the rotor position are related to the force Fourier coefficients through (2.4) to give

$$
\hat{h}_k = A(k) e^{i\gamma(k)} \hat{F}_k.
\tag{5.3}
$$

In (5.3), the amplitude and phase shift are determined as

$$
A(k) = \frac{\alpha}{\sqrt{\left(S_p - k^2\right)^2 + 4\zeta^2 S_p}} \quad \text{and} \quad \gamma(k) = -\tan^{-1}\left(\frac{2\zeta\sqrt{S_p}k}{(S_p - k^2)} \right).
\tag{5.4}
$$

In the absence of damping it is noted that the phase difference is zero, indicating that the rotor motion and force are in phase. Furthermore, the amplitude of the modified rotor position becomes singular if $S_p = k^2$, provided that the amplitude of the corresponding force Fourier coefficient and the coupling parameter are both non-zero. This behaviour corresponds with the trend observed using the asymptotic series analysis and indicates that in the undamped case, the $k = \sqrt{S_p}$th mode will be excited and tend to dominate. Figure 12(a) shows a plot of the undamped ($\zeta = 0$) amplitude $A(k)$ for a number of Fourier modes as a function of the spring stiffness and figure 12(b) is the corresponding case when the oscillations are damped ($\zeta > 0$). Comparing these figures it is seen that damping bounds the amplitude so that for $S_p = k^2$ the kth mode remains finite and also reduces the overall amplitude of the Fourier modes.

Additionally, damping brings about a phase shift given by (5.4) between the force and the rotor dynamics. From the nature of this expression, it is noted that a phase
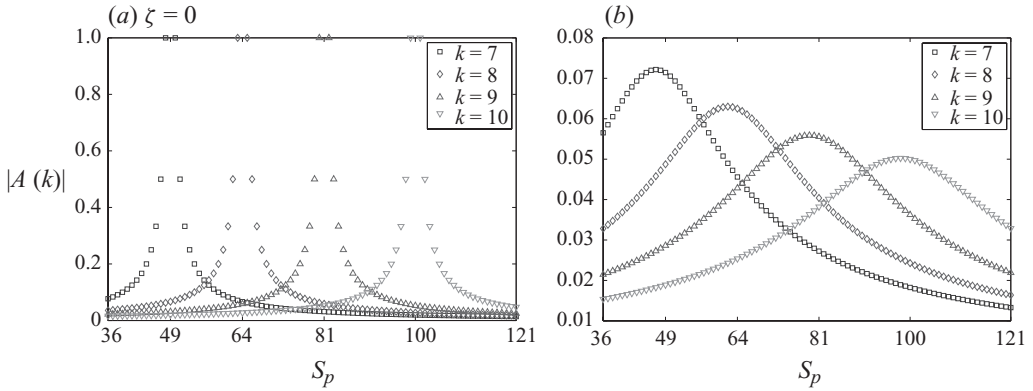
FIGURE 12. Approximate Fourier amplitude; $\alpha = 1$.

shift only appears because of damping, but the phase becomes singular for square values of the spring constant. Finally, it is observed that by decreasing the coupling parameter the amplitude of the rotor oscillations decreases, and in the case of zero coupling the rotor position remains at the equilibrium position because no forcing is applied to the system.

The use of this approximate Fourier analysis is restricted because the coupling of the force profile to the rotor position through the modified Reynolds equation is neglected. To incorporate the full coupled dynamics and the nonlinear behaviour due to large-amplitude disturbances, a full nonlinear numerical analysis is required.

5.3.2. *Numerical analysis for large-amplitude forcing*

Earlier results indicated that the most crucial bearing dynamics occur in the full nonlinear regime when the rotor–stator clearance becomes very small because of large-amplitude stator oscillations. The air–rotor–stator dynamics in this highly nonlinear case require detailed investigation because bearing failure due to rotor–stator contact is more likely to occur when the rotor–stator clearance is already reduced because of large-amplitude stator displacements. To observe the importance of nonlinear effects at the points where singular rotor dynamics occur, numerical solutions are computed for a range of different amplitude stator oscillations $0.1 \leqslant \epsilon \leqslant 0.9$. In the illustrative example considered, the spring constant is $S_p = 49$ and initially mechanical damping was included $\zeta = 1$.

In a classical non-forced system, the value of $\zeta = 1$ represents the point of critical damping: for values smaller or larger than one, the system will show oscillatory dynamics or monotonic damping, respectively. In the case of a forced system, such as the one considered here, it is possible to add to the transient behaviour of the system a solution of the corresponding non-forced system which sooner or later dies out. However, the forced solution does not die out, because it is driven by the loading force. In our case, we are looking at periodic solutions of the forced system where any transient (non-periodic) response has completely died out.

Figure 13(a) shows how the periodic rotor position profile increases for increasing amplitudes of stator oscillation ϵ. The stator is closest to the rotor at approximately $t = \pi/2$. For small amplitudes, the rotor displays an approximately uniform position and that only with $\epsilon \geqslant 0.7$ does the rotor position show significant displacements and is forced away from the approaching stator. Additional computations show this as a general feature for solutions at non-square values of the spring constant. However, on
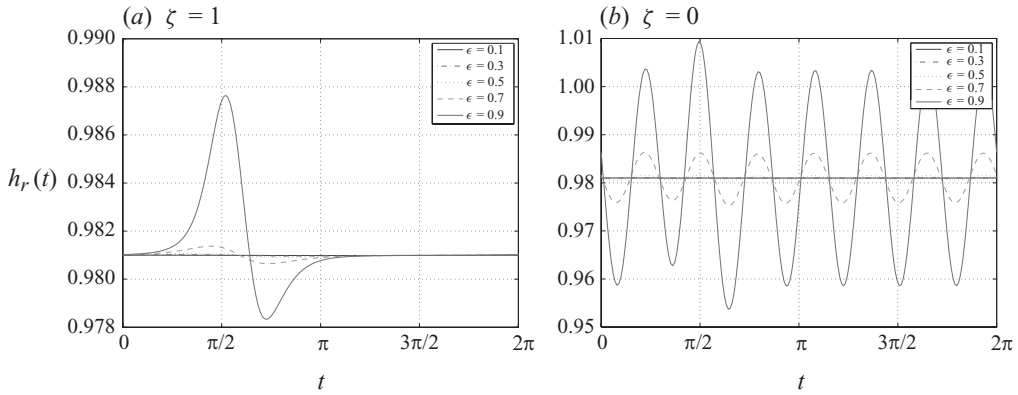
FIGURE 13. Numerical rotor position profiles; $\sigma = 0.001$, $\lambda = 5$, $S_p = 49$ and $\alpha = 1$.

the basis of the above analysis, it is expected that the rotor would display oscillations with a frequency of $k = 7$ for a stiffness of $S_p = 49$; however, in this case the higher-frequency oscillation is not present, indicating that the critical level of mechanical damping on the rotor has damped out the additional oscillation and constrained the motion.

The rotor position profile in the undamped case ($\zeta = 0$) in figure 13(b) displays a number of oscillations at a higher frequency than the forced stator motion superimposed upon the basic motion in figure 13(a). The additional component of the motion arises because of the excitation of the seventh Fourier mode, matching the predicted frequency of this oscillation. The figure shows that the nonlinear behaviour observed becomes significant for large-amplitude oscillations in the stator position having $\epsilon > 0.7$.

To observe the appearance of resonant dynamics more generally, the Fourier spectral collocation numerical scheme was used to compute the rotor dynamics at successive integer values of the spring constant. Figures 14(a) and 14(b) show the absolute value of the Fourier mode amplitudes for relevant modes plotted as a function of the spring constant for $\epsilon = 0.5$ and $\epsilon = 0.9$. In both figures, it is noticeable that peaks in the magnitude of the kth Fourier coefficient appear when $S_p = k^2$ and for stiffnesses away from a square number the amplitude decreases rapidly. Figure 14(b) also shows a number of secondary disturbances and peaks in the amplitude function even for spring constants far from the resonant value. The asymptotic expression for the rotor position given by (5.2) shows peaks in nearby modes that share a factor in the denominator of $(S_p - k^2)$. It is expected that the secondary behaviour seen in figure 14(b) is the result of similar characteristics in the full solution. The restricted nature of all the peaks in this undamped case is due to the bearing air flow imparting a damping force in the rotor through the forcing term that acts to stabilize the high-frequency rotor dynamics. To understand the appearance of resonant behaviour, it is noted that because the dimensionless stiffness parameter is $S_p = (\phi_0/\omega)^2$, integer values of $\sqrt{S_p}$ correspond to the rotor system having a natural frequency ϕ_0 that is an integer multiple of the forcing frequency ω, leading to resonant rotor behaviour.

The appearance of resonance in a mechanical system is undesirable because of the potential generation of unpredictable and destabilizing behaviour. Through the use of an arclength continuation method, the characteristics of a squeeze-film bearing are investigated in more detail to identify the effect of resonance.
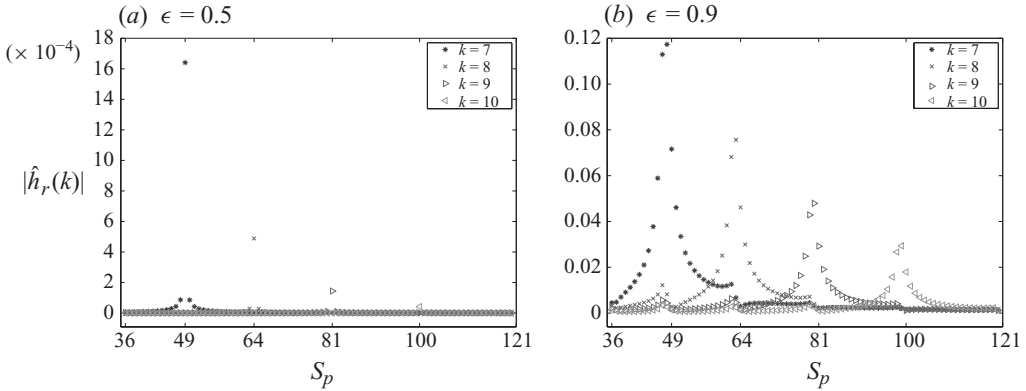
FIGURE 14. Numerical rotor Fourier coefficient plot; $\sigma = 0.001$, $\lambda = 5$, $\zeta = 0$ and $\alpha = 1$.
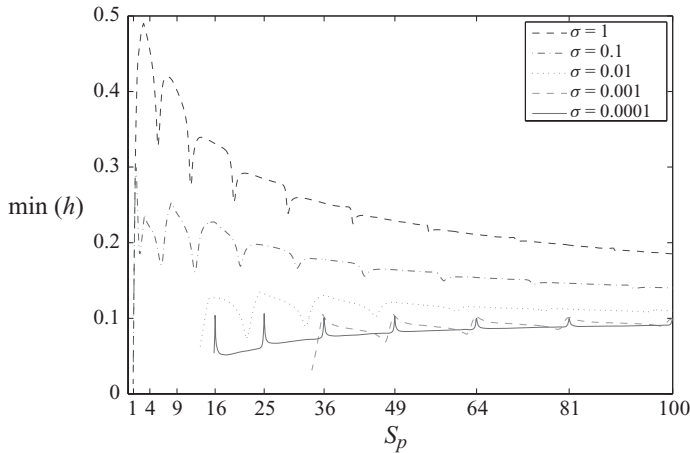

FIGURE 15. Minimum rotor–stator clearance plot from the arclength continuation solver; $\epsilon = 0.9$, $\lambda = 5$, $\zeta = 0$ and $\alpha = 1$.

A crucial feature of air-lubricated technology is that the bearing separation should be maintained. This requirement prompts the use of the minimum rotor–stator clearance as a characteristic measure of the solution dynamics. Figure 15 shows the minimum rotor–stator clearance plotted over a range of spring constants for several values of the squeeze number. The very low-frequency stator oscillation ($\sigma = 0.0001$) produces minimal film damping, and consequently a localized peak in the clearance is seen at each resonant point. For all non-resonant values, the minimum clearance uniformly reduces for reduced stiffness so that $\min(h_r) < 0.1$, the minimum clearance for a fixed rotor and a prescribed stator oscillation having amplitude $\epsilon = 0.9$. The reduced clearance is a result of the rotation drawing the rotor towards the stator.

For increased frequencies of oscillation, the minimum clearance increases as a larger squeeze-film force is developed that balances the effect of high-speed rotation. Interestingly, for these higher frequencies, it would be expected that the film displays increased damping characteristics to smooth out the resonant peaks; however, the resonant behaviour is still observed but reduces the clearance for the higher-frequency oscillations, a feature undesirable in bearing operation. Furthermore, the points where resonant peaks and troughs are observed are detuned for higher oscillation
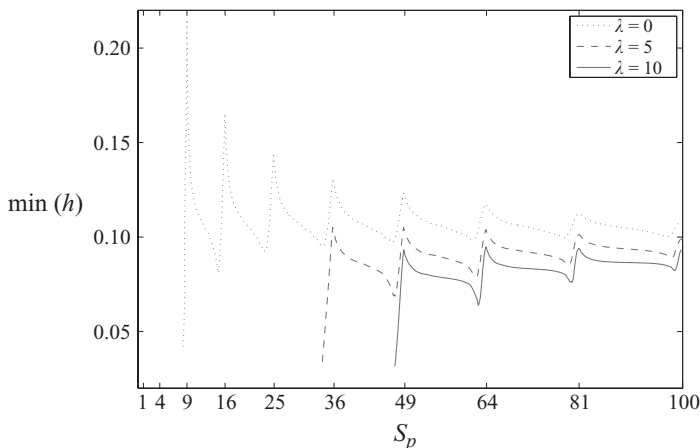
FIGURE 16. Minimum rotor–stator clearance from the arclength continuation solver; $\epsilon = 0.9$, $\sigma = 0.001$, $\zeta = 0$ and $\alpha = 1$.

frequencies so that they no longer occur for square values of the stiffness. Looking at the distribution of the troughs in the minimum clearance curve indicates that their distribution along the curve remains the same as previous results for $\sigma \ll 1$ but with a shift to smaller values of S_p, indicating that higher-frequency oscillations generate a degree of stiffness in the film.

To compare the bearing dynamics at different speeds of operation, results are shown in figure 16 for $\lambda = 0$, 5 and 10. The behaviour seen follows the results discussed above with a peak at each of the resonant values and then a trough, before increasing to the next resonant peak. It is noted that as the speed number increases, the minimum clearance decreases because of high-speed rotation. Additionally, the results show that for increased rotation speeds there is a critical resonant value that, for stiffnesses less than this value, leads the minimum clearance to tend to zero. For a further reduction in stiffness, no solution is found, showing that for this rotor stiffness the effect of high-speed rotation is not balanced and allows rotor–stator contact to occur.

The results computed using the arclength continuation method show generally smooth behaviour for non-resonant values of the spring constant. However, for values near a resonant value, the minimum clearance plots show a number of locations that are non-smooth. One of the characteristic features of the method of arclength continuation is that the solutions computed along a selected branch of solutions vary smoothly between steps. However, in this case the selected solution measure has non-smooth behaviour because the minimum clearance is determined by locating the critical point of the rotor–stator clearance. For a fixed rotor, the critical time point in a given period would always be $t = \pi/2$ due to the sinusoidal stator motion. However, if the position of the rotor varies, then this minimum can occur at a different location in the period. To explore this, the critical time point for the minimum clearance within a period is numerically identified for solutions from the arclength continuation numerical solver.

In figure 17 the continuous curve and the left-hand axis show the minimum clearance, and the thick discontinuous curve and the right-hand axis show the value of the critical time point t^* that corresponds to the minimum clearance calculated. For those points with non-resonant spring constants, the critical time value is approximately $t^* = \pi/2$. However, close to resonant values the critical
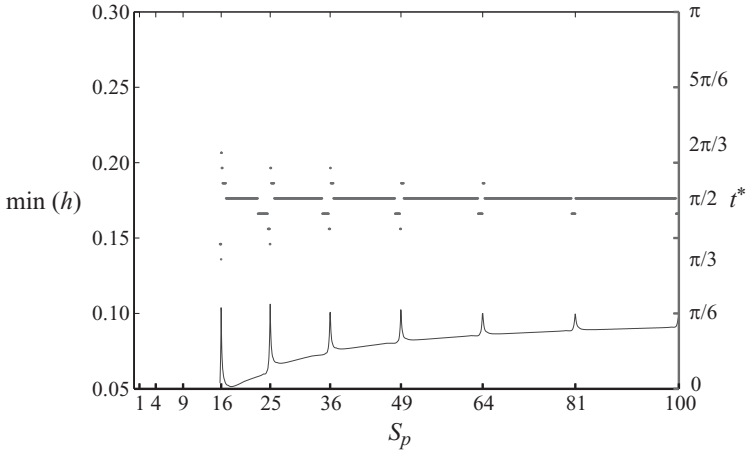
FIGURE 17. Minimum rotor–stator clearance and critical time points from the arclength continuation solver; $\epsilon = 0.9$, $\sigma = 0.0001$, $\lambda = 5$, $\zeta = 0$ and $\alpha = 1$.

time displays discontinuous behaviour, corresponding to the non-smooth points in the clearance curve. As the spring constant is reduced to near a resonant value, the critical time switches to later times in the period. However, when the spring constant is reduced past the resonant value, then the critical time value suddenly jumps again. After this jump, the critical time is significantly less than the original value of $t^* = \pi/2$, but as the stiffness is further reduced the critical value steps upwards to the original value.

Figure 18 shows similar features in the results for a higher-frequency stator oscillation, leading to more non-smooth points on the clearance curve, particularly for small stiffness values. This analysis confirms that the non-smooth behaviour of the minimum rotor–stator clearance is the result of discontinuities in the critical time point at which the minimum occurs and not due to numerical error.

To more clearly observe the discontinuous behaviour outlined above, figures 19–20 show the force–rotor–stator dynamics plotted for four different spring constants shown in figure 17 close to $S_p = 36$ computed using the method of arclength continuation. On the rotor and stator curves, the vertical line indicates the location of the critical time point within the period.

In figure 19(*a*), the rotor position shows a small-amplitude oscillation with an approximate frequency of six. For a slightly smaller spring constant, the results in figure 19(*b*) show that the critical time point has increased, resulting in the minimum clearance occurring later in the period. This minimum value corresponds to the stator being at almost maximum height and the critical time point being to the right-hand side of the second high-frequency rotor oscillation. Comparing this result with figure 20(*a*), where $S_p < 36$, it can be seen that the critical time point now occurs on the left-hand side of the second oscillation and also occurs before the maximum stator height is attained. There is no continuous transition from the location of the minimum clearance in these two cases. This result reinforces the understanding of the discontinuous behaviour seen in the critical time curve in figure 17 at each of the resonant spring constants. Examining figure 20(*b*) for a further reduced spring constant, it is seen that the critical time value has increased before eventually returning to $t^* = \pi/2$.
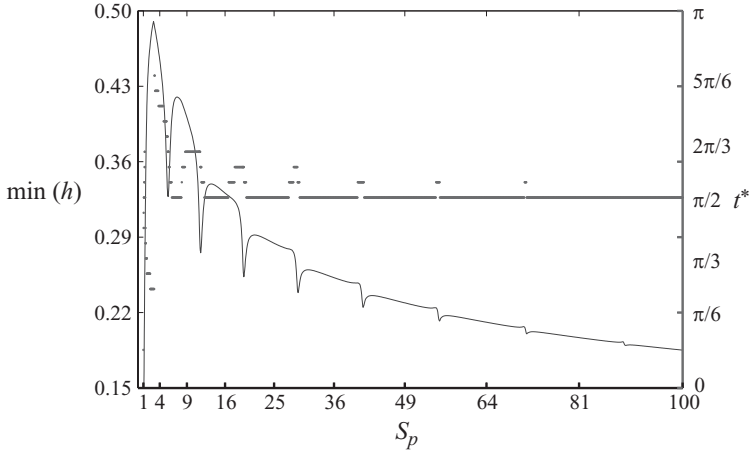
FIGURE 18. Minimum rotor–stator clearance and critical time points from the arclength continuation solver; $\epsilon = 0.9$, $\sigma = 1$, $\lambda = 5$, $\zeta = 0$ and $\alpha = 1$.
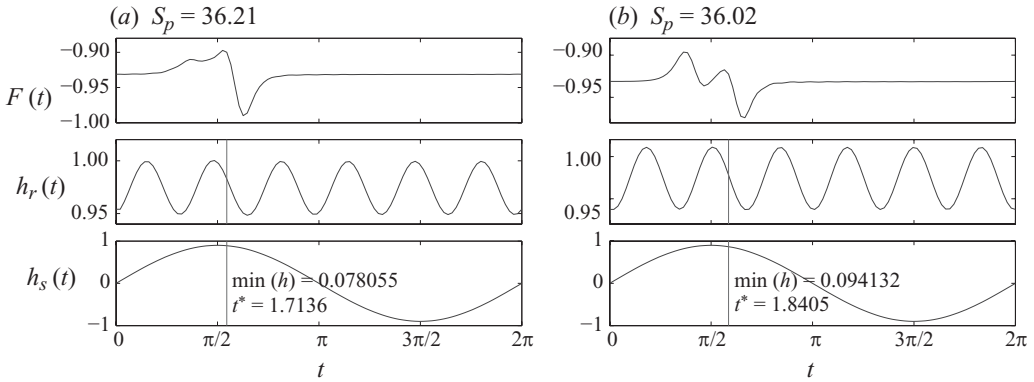

FIGURE 19. Force–rotor–stator dynamics from the arclength continuation solver; $\sigma = 0.0001$, $\epsilon = 0.9$, $\lambda = 5$, $\zeta = 0$ and $\alpha = 1$.
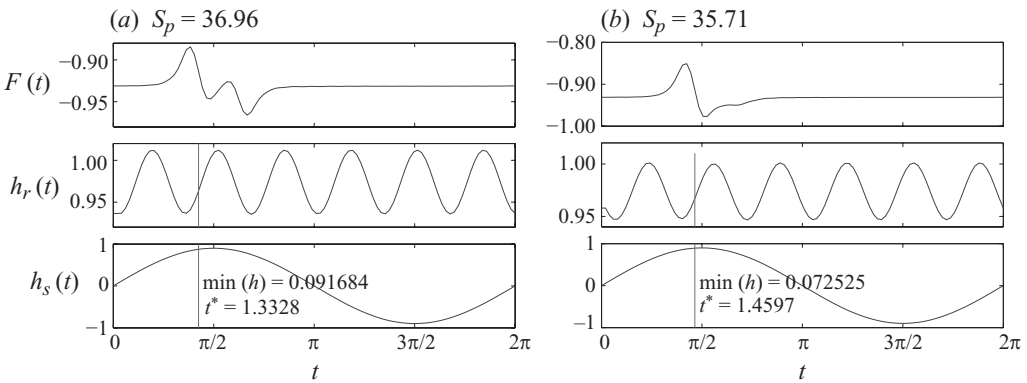

FIGURE 20. Force–rotor–stator dynamics from the arclength continuation solver; $\sigma = 0.0001$, $\epsilon = 0.9$, $\lambda = 5$, $\zeta = 0$ and $\alpha = 1$.

6. Summary and conclusions

A modified Reynolds equation model was introduced to simulate squeeze-film bearing dynamics with high-speed operation. The dynamics of two problems were modelled when the bearing stator is subject to a prescribed periodic oscillation, which is representative of physical disturbances. The first was the uncoupled problem of calculating the squeeze-film dynamics when the axial position of the rotor was fixed. The second problem was to determine the full air–rotor–stator behaviour when a forced spring-mass-damper model was used to model the coupled rotor motion

Initially the uncoupled squeeze-film dynamics were considered at low operating speeds. The asymptotic and analytical results for small-amplitude disturbances demonstrated that finite-amplitude forcing needed to be considered to gain a complete understanding of squeeze-film behaviour. Using a spectral collocation numerical scheme, the bearing force was seen to be a nonlinear function of the frequency and amplitude of the stator forcing. Extensions to high-speed bearing operation were investigated using the modified Reynolds equation model. A numerical computation showed that large-amplitude results were needed to fully observe the interaction between the rotation and the stator forcing properties but the effect of high-speed operation was a reduction in the load-carrying force.

A coupled air-flow–structure model provided a more general analysis of bearing behaviour. The effect of the stator forcing and rotor support parameters was identified through a numerical analysis. Results showed an effect of high-speed rotation was to draw the rotor and stator together, a feature opposed by the squeeze-film force that arises due to film compression. For the squeeze force to be significant, a combination of higher-frequency and larger-amplitude stator forcing is required. The mechanical damping and stiffness properties of the rotor support structure were seen to moderate the rotor motion.

An investigation of resonant rotor dynamics used asymptotic and Fourier analysis of the rotor motion for small-amplitude, low-frequency oscillations and numerical results for finite-amplitude oscillations. Resonance appeared in the rotor motion when the rotor stiffness took critical values for a range of operation speeds and forcing frequencies. Changes in the minimum rotor–stator clearance were presented as a function of the rotor stiffness to demonstrate the appearance of resonance. Non-smooth results were analysed and shown to be related to the location of the critical time value corresponding to the minimum clearance observed.

Appendix. Derivation of the modified Reynolds equation model

A dimensional analysis of the Navier–Stokes equations for compressible flow is established with typical air pressures and densities taken to be P (bar) and ρ_0 (kg m^{-3}), respectively. Typical radial, azimuthal and axial flow speeds are U (m s^{-1}), V (m s^{-1}) and W (m s^{-1}) and the radial variable is scaled using the bearing width R (m). The typical film thickness when the system is operating without any disturbance is h_0(m). The stator is forced with an oscillatory motion of frequency ω (Hz), suggesting that the time scale for the model is taken to be ω^{-1} (s).

To characterize the dimensionless flow properties, the radial and azimuthal Reynolds numbers are defined by (2.5). The Reynolds number ratio is given by (2.6). The aspect ratio is $\delta_0 = h_0/R$.

The importance of gravitational effects relative to the radial flow speed is parameterized by the Froude number

$$Fr = \frac{U}{\sqrt{gh_0}}. \tag{A 1}$$

Because the rotor is rotating at a rate Ω (r.p.s.), the azimuthal velocity is scaled using $V = \Omega R$ (m s^{-1}). Furthermore, the rigid surface boundary condition suggests that the axial velocity be scaled with $W = h_0/T = \omega h_0$ (m s^{-1}).

The radial component of the axisymmetric Navier–Stokes momentum equation becomes

$$Re_U \delta_0^2 \rho \left(\sigma \frac{\partial u}{\partial t} + u \frac{\partial u}{\partial r} + \sigma w \frac{\partial u}{\partial z} - (Re^*)^2 \frac{v^2}{r} \right) = -\frac{Ph_0^2}{\mu RU} \frac{\partial p}{\partial r} + \frac{\partial^2 u}{\partial z^2}$$
$$+ \delta_0^2 \left(\frac{1}{r} \frac{\partial}{\partial r} \left(r \frac{\partial u}{\partial r} \right) - \frac{u}{r^2} \right) + \delta_0^2 \frac{1}{3} \frac{\partial}{\partial r} \left(\frac{\partial}{\partial r}(ru) + \sigma \frac{\partial w}{\partial z} \right), \tag{A 2a}$$

the azimuthal component becomes

$$Re_U \delta_0^2 \rho \left(\sigma \frac{\partial v}{\partial t} + u \frac{\partial v}{\partial r} + \sigma w \frac{\partial v}{\partial z} + \frac{uv}{r} \right) = \frac{\partial^2 v}{\partial z^2} + \delta_0^2 \left(\frac{1}{r} \frac{\partial}{\partial r} \left(r \frac{\partial v}{\partial r} \right) - \frac{v}{r^2} \right), \tag{A 2b}$$

and the axial component becomes

$$Re_U \sigma \delta_0^4 \rho \left(\sigma \frac{\partial w}{\partial t} + u \frac{\partial w}{\partial r} + \sigma w \frac{\partial w}{\partial z} \right) = -\frac{Ph_0^2}{\mu RU} \frac{\partial p}{\partial z} + \sigma \delta_0^2 \frac{\partial^2 w}{\partial z^2}$$
$$+ \sigma \delta_0^4 \frac{1}{r} \frac{\partial}{\partial r} \left(r \frac{\partial w}{\partial r} \right) + \delta_0^2 \frac{1}{3} \frac{\partial}{\partial z} \left(\frac{\partial}{\partial r}(ru) + \sigma \frac{\partial w}{\partial z} \right) - \frac{Re_U \delta_0^2}{Fr^2} \rho, \tag{A 2c}$$

where the squeeze number is $\sigma = R\omega/U$. Similarly, the continuity equation becomes

$$\sigma \frac{\partial \rho}{\partial t} + \frac{1}{r} \frac{\partial}{\partial r}(\rho r u) + \sigma \frac{\partial}{\partial z}(\rho w) = 0. \tag{A 3}$$

Typically, the operation of air-lubricated technology involves design clearances of several microns. The radius of this configuration is usually in the range of 0.05–1 (m), suggesting that the aspect ratio is very small $\delta_0 \ll 1$, which is the key requirement for the lubrication approximation.

Using the viscous pressure scaling $P = \mu RU/h_0^2$ (bar) allows the momentum equations (A 2) to be reduced to leading order, giving the modified lubrication equations

$$-\lambda \frac{\rho v^2}{r} = -\frac{\partial p}{\partial r} + \frac{\partial^2 u}{\partial z^2}, \tag{A 4a}$$

$$0 = \frac{\partial^2 v}{\partial z^2}, \tag{A 4b}$$

$$0 = \frac{\partial p}{\partial z}. \tag{A 4c}$$

For highly rotating flows, the inclusion of the leading-order inertia term is parameterized by a speed parameter $\lambda = Re_U \delta_0^2 Re^{*2}$.

The equation of state is given by

$$p = K\rho, \tag{A 5}$$

with the modified gas constant $K = (\rho_0 k_b \tau h_0^2)/(\mu m_a R U)$, where $k_b \,(\mathrm{J\ K^{-1}})$ is the Boltzmann constant, $m_a \,(\mathrm{kg})$ is the mass of air and $\tau \,(\mathrm{K})$ is the fluid temperature.

The leading-order momentum equations (A 4) are solved, and applying no-slip conditions gives the radial and azimuthal velocities

$$u(r, z, t) = \frac{1}{2} \frac{\partial p}{\partial r} (z - h_s)(z - h_r)$$

$$- \frac{\lambda \rho r}{12 h^2} (z - h_s)(z - h_r)\left(z^2 + (h_r - 3h_s)z + 3h_s^2 - 3h_r h_s + h_r^2\right) \tag{A 6a}$$

and

$$v(r, z, t) = \frac{r}{h} (z - h_s). \tag{A 6b}$$

Integrating across the film thickness gives

$$\sigma \frac{\partial}{\partial t} (ph) + \frac{1}{r} \frac{\partial}{\partial r} \left(pr \int_{h_s}^{h_r} u \, \mathrm{d}z \right) = 0. \tag{A 7}$$

The radial velocity given by (A 6a) is integrated over the film thickness and through substitution into the above equation yields the axisymmetric modified Reynolds equation:

$$\sigma \frac{\partial}{\partial t} (ph) - \frac{h^3}{12r} \frac{\partial}{\partial r} \left(pr \frac{\partial p}{\partial r} \right) + \frac{\lambda}{40K} \frac{h^3}{r} \frac{\partial}{\partial r} \left(r^2 p^2 \right) = 0. \tag{A 8}$$

REFERENCES

AGRAWAL, G. L., PATEL, K. H. & MUNSON, J. H. 2007 (August 28) Hydrodynamic foil face seal. United States Patent 7,261,300 B2.

BELFORTE, G., RAPARELLI, T. & VIKTOROV, V. 1999 Theoretical investigation of fluid inertia effects and stability of self-acting gas journal bearings. *J. Tribol.* **121**, 836–843.

BLECH, J. J. 1983 On isothermal squeeze-films. *J. Lubr. Technol.* **105**, 615–620.

BRUNETIÈRE, N. & TOURNERIE, B. 2006 The effect of inertia on radial flows: application to hydrostatic seals. *J. Tribol.* **128**, 566–574.

BRUNETIÈRE, N., TOURNERIE, B. & FRÊNE, J. 2002 Influence of fluid flow regime on performances of non-contacting liquid face seals. *J. Tribol.* **124**, 515–523.

BRUNETIÈRE, N., TOURNERIE, B. & FRÊNE, J. 2003a TEHD lubrication of mechanical face seals in stable tracking mode. Part 1. Numerical model and experiments. *J. Tribol.* **125**, 608–616.

BRUNETIÈRE, N., TOURNERIE, B. & FRÊNE, J. 2003b TEHD lubrication of mechanical face seals in stable tracking mode. Part 2. Parametric study. *J. Tribol.* **125**, 617–627.

CLIFFE, K. A., SPENCE, A. & TAVENER, S. J. 2000 The numerical analysis of bifurcation problems with applications to fluid mechanics. *Acta Numer.* **9**, 39–131.

DELLACORTE, C. & VALCO, M. J. 2000 Load capacity estimation of foil air journal bearings for oil-free turbomachinery applications. *Tribol. Trans.* **43**, 795–801.

DOWSON, D. 1961 Inertia effects in hydrostatic thrust bearings. *J. Basic Engng* **83**, 227–234.

FOURKA, M., TIAN, Y. & BONIS, M. 1996 Prediction of the stability of air thrust bearings by numerical, analytical and experimental methods. *Wear* **198**, 1–6.

GARRATT, J. E., CLIFFE, K. A., HIBBERD, S. & POWER, H. 2010 A numerical scheme for solving the periodically forced Reynolds equation. *Intl J. Numer. Methods Fluids* (submitted).

GROSS, W. A. 1980 *Fluid Film Lubrication*. Wiley.

HASEGAWA, E. & IZUCHI, H. 1982 Inertia effects due to lubricant compressibility in a sliding externally pressurized gas bearing. *Wear* **80**, 207–220.

HESHMAT, C. A., XU, D. S. & HESHMAT, H. 2000 Analysis of gas lubricated foil thrust bearings using coupled finite element and finite difference methods. *J. Tribol.* **122**, 199–204.

KELLER, H. B. 1977 Numerical solution of bifurcation and nonlinear eigenvalue problems. In *Applications of Bifurcation Theory* (ed. P. H. Rabinowitz), pp. 359–384. Academic Press.

LANGLOIS, W. E. 1962 Isothermal squeeze-films. *Q. Appl. Math.* **20**, 131–150.

MALANOSKI, S. B. & WALDRON, W. 1973 Experimental investigation of air bearings for gas turbine engines. *ASLE Trans.* **16** (4), 297–303.

MINIKES, A. & BUCHER, I. 2003 Coupled dynamics of a squeeze-film levitated mass and a vibrating piezoelectric disk: numerical analysis and experimental study. *J. Sound Vib.* **263**, 241–268.

MUNSON, J. & PECHT, G. 1992 Development of film riding face seals for a gas turbine engine. *Tribol. Trans.* **35**, 65–70.

PARKINS, D. W. & STANLEY, W. T. 1982 Characteristics of an oil squeeze-film. *J. Lubr. Technol.* **104**, 497–502.

POPPER, B. & REINER, M. 1956 The application of the centripetal effect in air to the design of a pump. *Br. J. Appl. Phys.* **7**, 452–453.

SALBU, E. O. J. 1964 Compressible squeeze-films and squeeze bearings. *J. Basic Engng* **86**, 355–366.

SAN ANDRÉS, L. & KIM, T. H. 2009 Analysis of gas foil bearings integrating FE top foil models. *Tribol. Intl* **42**, 111–120.

STOLARSKI, T. A. & CHAI, W. 2006a Load-carrying capacity generation in squeeze-film action. *Intl J. Mech. Sci.* **48**, 736–741.

STOLARSKI, T. A. & CHAI, W. 2006b Self-levitating sliding air contact. *Intl J. Mech. Sci.* **48**, 601–620.

STOLARSKI, T. A. & CHAI, W. 2008 Inertia effect in squeeze-film air contact. *Tribol. Intl* **41**, 716–723.

TAYLOR, G. & SAFFMAN, P. G. 1957 Effects of compressibility at low Reynolds number. *J. Aeronaut. Sci.* **24**, 553–562.

TREFETHEN, L. N. 2000 *Spectral Methods in Matlab*. Wiley.

WITELSKI, T. P. 1998 Dynamics of air bearing sliders. *Phys. Fluids* **10**, 698–708.